Mamlouk M, Scott K.

A boron phosphate-phosphoric acid composite membrane for medium temperature proton exchange membrane fuel cells.

***Journal of Power Sources* 2015, 286, 290-298.**

Journal of Power Sources 286 (2015) 290–298

Contents lists available at ScienceDirect

Journal of Power Sources

journal homepage: www.elsevier.com/locate/jpowsour

A boron phosphate-phosphoric acid composite membrane for medium temperature proton exchange membrane fuel cells

M. Mamlouk*, K. Scott

School of Chemical Engineering and Advanced Materials, Merz Court, University of Newcastle, Newcastle Upon Tyne NE1 7RU, United Kingdom

HIGHLIGHTS

- A composite membrane based on BPO_4 with excess of PO_4.
- Platinum micro electrode was used to study the electrolyte ORR compatibility.
- Conductivity of the self-supported electrolyte was 7.9×10^{-2} S cm^{-1} at 150 °C/5%RH.
- Fuel cell tests showed a major enhancement in performance of BPO_x over H_3PO_4-PBI.
- Current densities at 0.6 V were 706 for BPO_x and 425 mA cm^{-2} for 5.6H_3PO_4-PBI.

ARTICLE INFO

Article history:
Received 6 January 2015
Received in revised form
25 March 2015
Accepted 28 March 2015
Available online 31 March 2015

Keywords:
Boron phosphate
PBI
HT-PEMFCs
Composite membrane
Medium temperature

ABSTRACT

A composite membrane based on a non-stoichiometric composition of BPO_4 with excess of PO_4 (BPO_x) was synthesised and characterised for medium temperature fuel cell use (120–180 °C). The electrolyte was characterised by FTIR, SS-NMR, TGA and XRD and showed that the B–O is tetrahedral, in agreement with reports in the literature that boron phosphorus oxide compounds at B:P < 1 are exclusively built of borate and phosphate tetrahedra. Platinum micro electrodes were used to study the electrolyte compatibility and stability towards oxygen reduction at 150 °C and to obtain kinetic and mass transport parameters. The conductivities of the pure BPO_x membrane electrolyte and a Polybenzimidazole (PBI)-4BPO_x composite membrane were 7.9×10^{-2} S cm^{-1} and 4.5×10^{-2} S cm^{-1} respectively at 150 °C, 5%RH.

Fuel cell tests showed a significant enhancement in performance of BPO_x over that of typical 5.6H_3PO_4-PBI membrane electrolyte. The enhancement is due to the improved ionic conductivity (3×), a higher exchange current density of the oxygen reduction (30×) and a lower membrane gas permeability (10×). Fuel cell current densities at 0.6 V were 706 and 425 mA cm^{-2} for BPO_x and 5.6H_3PO_4-PBI, respectively, at 150 °C with O_2 (atm).

1. Introduction

Increasing the operating temperature of polymer electrolyte membranes fuel cell above 100 °C is highly desirable [1]. This will result in several advantages: faster reaction rates at both electrodes, anode and cathode, an improved CO tolerance leading to a simplified fuel pre-treatment [2–4], higher ionic conductivity can be achieved and improved heat and power cogeneration [5].

Research on proton exchange membranes for medium temperature (120–180 °C) PEMFCs operating under low humidity is usually focused on polybenzimidazole based membranes. PBI is typically doped with phosphoric acid to provide proton conductivity [3,6]. Sulphuric acid [7] and ionic liquids [8] have been used to replace phosphoric acid; however these resulted in poorer performances. Phosphoric acid has specific properties making it a desirable candidate for medium temperature electrolytes:excellent thermal, chemical and electrochemical stability at fuel cells' conditions and low vapour pressure at temperatures above 150 °C [9].

However, limitations include deactivation via phosphate anion adsorption at positive potentials [6,10] and acid leaching.

Other approaches have utilised organic/inorganic membrane composites using phosphoric acid as an electrolyte with 1H-1,2,3-triazole grafted alkoxy silanes and tetraethoxy silane (TEOS) [11], 3-glycidoxypropyltrimethoxysilane (GPTMS) and 3-aminopropyltriethoxysilane (APTES) [12] or zirconia and zeolite [13] to produce self-supporting membranes.

* Corresponding author.
E-mail address: mohamed.mamlouk@ncl.ac.uk (M. Mamlouk).

http://dx.doi.org/10.1016/j.jpowsour.2015.03.169

While research often is focuses on the ionic conductivity of the developed membranes, the compatibility of the electrolyte for fuel cell application is of utmost importance, and includes factors such as: conductivity, thermal stability, electrochemical stability and compatibility with the catalyst under reducing and oxidizing potentials and O_2/H_2 permeability. Electrolyte permeability to gases also strongly influences mass transport of electro-active species and hence influences electrode reaction kinetics [14]. While pristine PBI is considered a good candidate for membrane materials due to its low gas permeability, addition of PBI to the catalyst layer for proton conduction could impose mass transport limitation on anode and cathode performances, depending on the thickness of the polymer film formed on the catalyst sites and the amount of phosphoric acid doped in the PBI required to facilitate proton conduction. The higher the doping level used, the higher the conductivity would be, but mechanical properties, such as tensile stress of PBI deteriorate dramatically due to increased swelling. High swelling will also cause a significant increase in permeability and hydrogen cross-over of around 5 mA cm^{-2} [15] and produce an open circuit voltage of around 0.85 V [16]. A balance between conductivity and mechanical properties was achieved at doping level of c.a. 5.6 acid per repeat PBI unit (PRU) [17]. Doping level will also affect significantly the electrode performance due to acid mobility from the membrane to the electrodes.

At doping level of 5.6 PRU the ionic conductivity is ca 4.5×10^{-2} S cm^{-1} (150 °C, 3%RH) [18]. There is a need to improve the membrane conductivity to around 8×10^{-2} to minimise IR losses and obtain membrane conductivities similar to Nafion®. This can be accomplished by a larger phosphoric acid content in the membrane but without increase in permeability and swelling. One way to achieve this is via composite membranes.

PBI membranes with high acid doping of 6 PRU means that there is a large quantity of free mobile acid available to flood the catalyst layer. To ressolve this changes in the anode and cathode structures is required. These include the use of thicker catalyst layer, utilising lower Pt/C ratio (20–30% wt) and increased de-wetting by increasing the Teflon content to 40% wt [19]. Another limitation is the chemical stability of the PBI membranes which degrades at temperature above 150 °C due to dehydration of phosphoric acid and other environmental issues [20].

In boron phosphate BPO_4 both P^{+5} and B^{+3} are tetrahedrally coordinated by oxygen. The structure of stoichiometric boron phosphate is similar to that of cristobalite, containing alternate PO_4 and BO_4 tetrahedrally linked by shared oxygen atoms forming a three dimensional network [21,22]. While BPO_4 is only partially soluble or insoluble in water (depending on preparation temperature), its conduction mechanism at low temperatures is significantly dependant on humidity, i.e. liquid phase conduction involving H_3PO_4 molecules [23] (10^{-7} S cm^{-1} at 0%RH to 4.8×10^{-2} S cm^{-1} at 100%RH) where the surface layers of the solid BPO_4 are rendered mobile by the hydrolysis and dissolution in water resulting in several species including phosphoric acid [24]. Composites of organic/inorganic membranes with BPO_4 and sulphonated polyetheretherketone (SPEEK) up to 40% wt lead to improved membrane properties [25,26], composite of BPO_4 and PBI-SPEEK gave maximum conductivity at 20% wt BPO_4 of 6×10^{-3} S cm^{-1} [26].

The non-stoichiometric composition of BPO_4 with excess of PO_4 units (B/P 0.8) increases its conductivity [23]. We propose a composite membrane (BPO_x) based on non-stoichiometric composition of BPO_4 with significant excess of PO_4 (B/P: 0.25). The excess phosphoric acid will facilitate proton conduction in the temperature range of 100–200 °C in the absence of water, while BPO_4 will provide a three dimensional network with PO_4 resulting in a composite membrane.

2. Experimental

2.1. Materials and BPO_x

Boric acid (>99.5%, Sigma), ortho phosphoric acid (reagent grade, Fisher) and dimethyl sulfoxide DMSO (>99.5%, Sigma) were used as received.

BPO_x samples with B/P atomic ratios 0.25 have been prepared from ortho-phosphoric acid and boric acid. Applicable amounts of the acids (4 mol H_3PO_4:1 mol H_3BO_3) were stirred continuously in a ceramic pan at 250 °C in air until a thick white slurry was obtained. The obtained slurry was then kept at the same temperature without stirring for 6 h. The samples were then transferred to sealed glass bottles to prevent humidity adsorption from the atmosphere. After cooling, the samples solidified and were ground and pressed using a 32 mm stainless steel pellet die (Fluxana, Germany) at 10 tonnes, producing 150 μm composite membrane discs.

2.2. Preparation of PBI/PBO_x hybrid membranes

Poly(2,2′-m-(phenylene)-5,5′-bibenzimidazole) PBI powder was dissolved in DMSO. The composite membranes were fabricated using a solution casting method [8]. An appropriate amount of BPO_x was added to the PBI/DMSO solution (3 wt%) to produce 3 and 4 PRU [moles BPO_X per mole PBI], resulting in a viscous gel-like solution after stirring, due to the interaction between PBI and PBO_x. The mixture was sonicated for several hours and placed in a water bath at 75 °C for 12 h. The obtained viscous solutions were cast on a Petri dish in an open oven at 80 °C for 12 h. The uniform composite hybrid membranes were peeled from the Petri dish and dried further in an oven at 110 °C for 4 h before starting the measurements. Attempts to prepare membranes with higher BPO_x content were not successful as the filler content become too high with respect to the polymer (PBI) and cracked membranes were obtained.

Impregnation method was also investigated to prepare PBI/BPO_x membranes. PBI membranes obtained from PBI/DMSO solution 3 wt%, were immersed in saturated solution of the prepared BPO_x in DMSO, DMAc, H_2O and methanol at 60 °C for one week. The resulting membranes had very low electrolyte uptake (max 0.9 PRU) and therefore low conductivity, which is mainly due to the low solubility of the prepared BPOx in the studied solvents. BPO_4 prepared at temperature of 250 °C has ca 50% soluble part when 1 wt% slurry in water was tested for 15 h [23].

2.3. BPO_x characterisation

FTIR spectra of the membranes samples were measured with a Varian 800 FT-IR spectrometer system in the range of 4000–600 cm^{-1} with a resolution of 2 cm^{-1}. The KBr pellet method was employed for solid samples.

^{11}B and ^{31}P Solid state MAS NMR spectra were obtained using Varian VNMRS spectrometer (EPSRC UK National Solid-state NMR Service at Durham). Direct excitation: frequency and acquisition time of 128.3 Hz, 30 ms and 161.9 Hz, 50 ms, respectively. References: BF_3/OEt_2 and 85% H_3PO_4.

XRD pattern was collected using the PANalytical X'Pert Pro diffractometer using the X'Celerator area detector, Cu K X-rays were used.

Thermal stability of the prepared PBO_x samples was investigated by thermogravimetric analysis (Perkin Elmer, TGA 4000). The samples were heated from room temperature to 500 °C with a heating rate of 5 °C/min under nitrogen atmosphere. Weight loss was measured and reported as a function of temperature.

Differential scanning calorimetric (DSC) was also performed under a nitrogen atmosphere. The samples were placed and compacted in open alumina pans.

2.4. Conductivity

Through plane ionic conductivities of the composite membranes were determined by means of complex impedance analysis in the temperature range of 60–180 °C. The two point technique (through plane) used two platinum probes (25 mm × 5 mm) in contact with opposite sides of the measured material. The electrochemical measurements were carried out with an Autolab PGSTAT 30 (Eco Chemie, The Netherlands). The frequencies were scanned from 200 kHz to 1 Hz recording six points per decade with an AC signal amplitude of 15 mV. The relative humidity was obtained from an intrinsically safe humidity sensor (Vaisala HUMICAPVR, Finland). The conductivity (σ) was calculated as follows:

$$\sigma = \frac{L}{RA} \quad (1)$$

where R, L, and A are the measured resistance, membrane thickness, and cross-sectional area of the membrane, respectively.

The membranes were dried in an oven at 110 °C for 4 h prior to testing. The dry measurements were carried out between 60 and 150 °C, beyond which two different humidities of 5 and 3% were introduced for temperatures of 150 and 180 °C, respectively.

2.5. Macro electrode studies

BPO_x is a solid crystal at room temperature, and at 150 °C in on humidification it turns to a viscous slurry which enables its characterization in a three electrode cell. Most reported kinetic studies are made using RDE studies which restrict the measurement to low temperatures and dilute solutions far removed from the conditions used in practical fuel cells. A three electrode cell using Pt electrode was used to measure the ORR kinetic parameters and the electrolyte permeability of BPOx and 85% H_3PO_4 at 150 °C. A 250 μm Pt macro electrode (BASi, USA) was selected for the tests at 150 °C in order to obtain currents in the range of 10^{-9}–10^{-8} A [27] (minimum range available with the used Autolab PGSTAT 302N). 500 μm Pt macro electrode was also used (in the case of H_3PO_4) for comparison. A 0.5 mm Pt wire was used as the counter electrode, and the reference electrode was an in-house made reversible hydrogen electrode in 85% H_3PO_4 connected to the studied electrolyte by lugging capillary terminated by Vycor glass frit. The studied electrolytes were saturated by oxygen and air prior to tests. Linear sweep voltammetry were conducted at 1 mV s^{-1} and cyclic voltammogram at 500 and 200 mV s^{-1}. Chronoamperometry measurements were run at 0.2 V (RHE) and recorded over 180 s with interval of 0.1 s.

Chronoamperometry at a disk electrode also leads to steady-state currents at infinite times. By combining measurements in the time-dependent and steady-state domains, the oxygen solubility and diffusion can be calculated. The exact solution is an infinite series, which, for sufficiently long times ($\tau = 4Dt/r^2 > 3.2$ for 1% accuracy) reduces to [28]:

$$I = \left(\frac{8}{\pi^2}\right)\frac{nFAC\sqrt{D}}{\sqrt{\pi t}} + 4nFDcr \quad (2)$$

where A is the electrode area, n electron number, F faraday constant, C oxygen solubility, D oxygen diffusion and t is the time since the potential step.

2.6. Fuel cell

A1 cm^2 titanium cell with a gold plated serpentine flow fields and O-ring seal was used for the fuel cell tests. The temperature of the cell was controlled by thermostatically controlled cartridge heaters inserted into the cell body. The electrochemical measurements was recorded by an Autolab PGSTAT 302N potentiostat (Eco Chemie, The Netherlands). Polarization curves were recorded using a cathodic sweep at a scan rate of 2 mV s^{-1}.

The catalyst ink was prepared by sonicating the Pt (20, 30, 40 & 50%Pt/C, Johnson Matthey) catalyst and polytetrafluoroethylene (PTFE) dispersion (60 wt% Aldrich) in a water–ethanol mixture. The ink was sprayed under nitrogen on Freudenberg (FFCCT, Germany) gas diffusion electrodes with wet proofed micro porous layer. Typical anodes (20% Pt/C) and cathodes (30, 40 or 50%Pt/C) were prepared using 0.2 and 0.4 mg_{Pt} cm^{-2} with 40% wt PTFE, respectively as explained elsewhere [9,19,29]. $\lambda_{H2} = 1.2$ and $\lambda_{air} = 2$.

3. Result and discussion

3.1. Characterization of non-stoichiometric BPO_4, (B/P 0.25)

3.1.1. Infrared study

FTIR spectra of the non-stoichiometric BPO_4, (B/P 0.25) are shown in Fig. 1A. Peaks at 1647 and 3374 cm^{-1} correspond to HOH bending and OH stretching from free water adsorbed from atmospheric humidity.

There are no peaks observed in the range of 1300–1500 cm^{-1}, attributed to asymmetric trigonal B–O stretching [30]. This suggests that the B–O is tetrahedral, in agreement with reports in the literature that boron phosphorus oxide compounds at B:P < 1 are exclusively built of borate and phosphate tetrahedra and do not contain boron in a trigonal planar coordination [31]. This is also confirmed by the first peak at 1030 cm^{-1} in the range of 1100–850 cm^{-1} assigned to asymmetric tetrahedral B–O stretching and second peak at 744 cm^{-1} in the range of 850–700 cm^{-1} assigned to symmetric tetrahedral B–O stretching [32]. The Peak at 619 cm^{-1} is assigned to O–B–O bending.

The IR peak at 878 cm^{-1} is attributed to symmetric P–O stretching and the peaks at 904 & 971 cm^{-1} are from asymmetric P–O stretching [33,34].

The IR spectrum of boron phosphate is reported [22] to contain O–B–O bending, asymmetric P–O stretching and asymmetric tetrahedral B–O stretching which were all observed as described above.

3.1.2. Thermal properties

The thermal stability of BPO_x membranes was studied at the intended operating temperature range above 100 °C. Thermal gravimetric analysis (TGA) and differential scanning calorimetry (DSC) curves are shown in Fig. 1B. It can be seen that there was no weight loss from the BPO_x sample up to 150 °C (0.4% wt); indicating that the materials are very stable even under non-humidified conditions. Beyond 150 °C, a slow weight loss started and levelled off at *ca* 500 °C at 15% wt. This weight loss can be assigned to the dehydration and dimerization of phosphoric acid groups forming meta-phosphate and other higher phosphates [19]:

$$\text{First stage}: \ 2H_3PO_4 \leftrightarrow H_4P_2O_7 + H_2O\uparrow \quad (3)$$

$$\text{Second stage}: \ H_4P_2O_7 + H_3PO_4 \leftrightarrow H_5P_3O_{10} + H_2O\uparrow \quad (4)$$

The DSC data shows two characteristic peaks at *ca*. 107 and 210 °C as reported in the literature for BPO_4 [21].

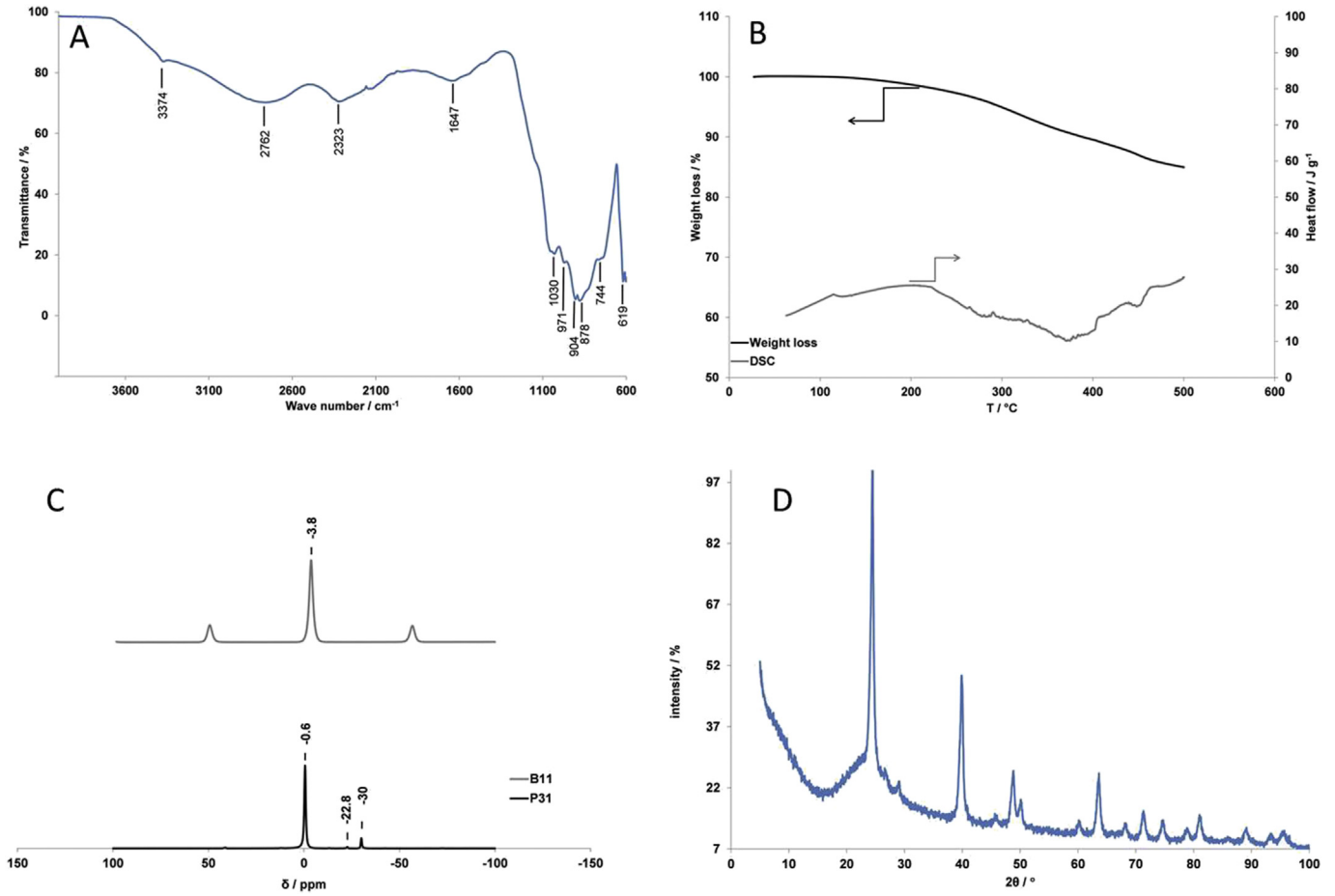

Fig. 1. (A) FTIR spectra of the BPO_x measured in the range of 4000–600 cm^{-1} with a resolution of 2 cm^{-1} (B). TGA and DSC of the prepared BPO_x samples heated from room temperature to 500 °C with a heating rate of 5 °C/min under nitrogen atmosphere. (C). ^{11}B and ^{31}P Solid state MAS NMR spectra for the prepared BPO_x (D). XRD pattern of the prepared BPO_x using Cu K X-rays with $\lambda = 1.54180$ Å.

3.1.3. Solid state MAS NMR

^{31}P and ^{11}B MAS NMR spectra of the prepared BPO_x (B/P: 0.25) are shown in Fig. 1C.

There is one ^{11}B symmetric line at −3.7 ppm (plus spinning sidebands) confirming that there is only one boron environment and it has a tetrahedral symmetry. This is in agreement with the FTIR results discussed earlier.

The ^{31}P signal at −30 ppm is assigned to tetra-coordinated PO_4 species in BPO_4 with spinning sidebands at −72 and +12 ppm (hardly visible) associated with it, while the signal at −22.8 ppm is assigned to partially hydrolysed boron phosphate [23,24] as shown below:

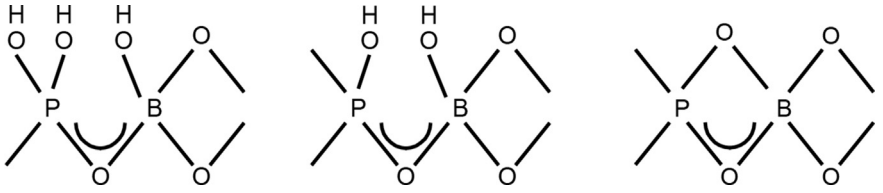

(5)

The ^{31}P signal at −0.6 ppm has the largest intensity and is assigned to H_3PO_4 species (^{11}P measurement is referenced versus 85wt% H_3PO_4). This large intensity H_3PO_4 species signal is reported for BPO_4 with a calcination degree of 400 °C and below and attributed to the partial solubility of BPO_4 (hydrolysis to H_3PO_4) [23].

3.1.4. XRD pattern

The powder X-ray diffraction patterns of the prepared BPO_x (B/P: 0.25) sample are shown in Fig. 1D. All the peaks in the X-ray powder pattern belong to tetragonal BPO_4. The XRD pattern was a perfect match with the JCPDS reference code: 00–034-0132 and other literature [22] for boron phosphate, with tetragonal structure and crystallographic parameters of a: 4.3425 Å and c: 6.6415 Å.

3.1.5. Conductivity of BPO_x and PBI composites

Through plane conductivities for the prepared BPOx (B/P: 0.25)

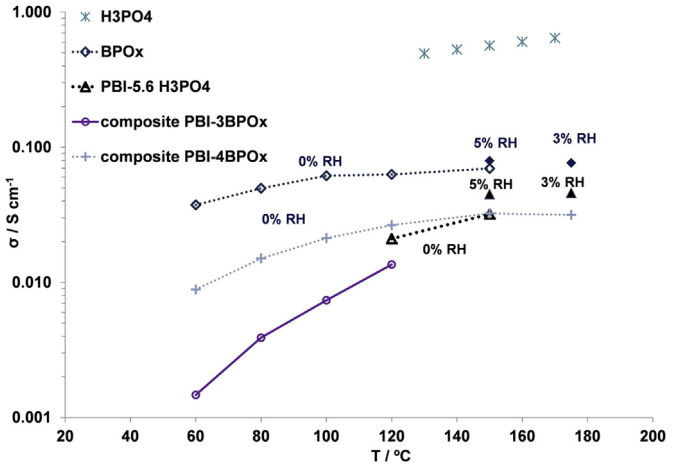

Fig. 2. Through plane ionic conductivities of BPO_x pellets, BPO_x-PBI composite membranes, H_3PO_4 [36] and PBI-5.6H_3PO_4 [18,35] in the temperature range of 60–180 °C and humidity range from 0 to 5%.

membrane and its composite with PBI of 3 and 4PRU (57wt% and 66wt%, respectively) areas shown in Fig. 2. The conductivity of PBI-5.6H_3PO_4 [18,35] and that of 85wt% H_3PO_4 [36] is shown for comparison.

Reported conductivity data for at 40%wt BPO_4 with SPEEK-PBI composite was 4×10^{-3} S cm^{-1} at room temperature [26]. Pure BPO_4 showed an increased conductivity with decreasing B/P ratio and decreased calcination temperature. The highest conductivity reported at room temperature for calcination temperature of 410 °C and B/P:0.8 of ca. 6×10^{-2} S cm^{-1} at 20% RH [23]. The lower calcination temperature of 250 °C and the significantly lower B/P ratio of 0.25 used, as well as the higher testing temperature of 150 °C, are the reasons behind the observed high ionic conductivity. BPO_x (B/P:0.25) showed ionic conductivity of 7×10^{-2} and 8×10^{-2} S cm^{-1} at 150 °C and dry and 5% RH, respectively. This translates to a resistivity value of 187 mΩ cm^2 (considering the prepared membrane thickness of 150 μm) very similar to the value of that of PBI 5.6H_3PO_4 of 167 mΩ cm^2 considering 50 μm and conductivity of 3×10^{-2} S cm^{-1} at 150 °C.

These results are very promising and similar to those of Nafion at operating conditions of 80 °C and 100% RH. This material will therefore be investigated further in terms of suitability for ORR in a three electrode cell and fuel cell. The conductivity range of BPO_x (B/P:0.25) lies in the middle of the range between pure phosphoric acid and that of PBI doped with 5.6 PRU phosphoric acid. This is because BPO_x contains a higher phosphoric acid volume fraction in comparison to 5.6 PRU phosphoric acid and consequently higher conductivity. In fact the conductivity is higher than that of PBI-8PRU at the same conditions [37].

The ionic conductivity for the prepared PBI composite membranes increased with increasing BPO_x content, with a maximum conductivity of 3×10^{-2} S cm^{-1} achieved with 66 wt % at 150 °C and dry atmosphere. The latter value is very similar to the PBI-5.6H_3PO_4 conductivity at the same conditions. However, the mechanical property of the composite membrane with such high filler content is very poor and normally the BPO_4 content is limited to 40%wt [26].

3.2. Macro electrode studies

3.2.1. Cyclic voltammogram

When comparing the activity of catalyst surfaces, knowledge of the catalyst electrochemical surface area (ESA) is essential. The commonly used electrochemical technique for the determination of metal electrode active surface area is anodic stripping of hydrogen adsorbed in the under-potential deposition potential (UPD) region. This corresponds to the total charge passed during hydrogen adsorption/desorption after accounting for the double layer capacity. An average value of 210 μC cm^{-2} of the real electrode surface for a clean smooth platinum electrode was considered in the calculation here. Fig. 3A shows the cyclic voltammogram of two Pt macro electrodes (Ø = 500 and 250 μm) in H_3PO_4 and BPO_x at 500 mV s^{-1}. The voltammogram has the typical characteristic of Pt in acidic media; H adsorption/desorption, double layer, oxygen species adsorption/desorption, for both H_3PO_4 and BPO_x at 150 °C. No other peaks (oxidation or reduction) were visible and there was no anodic or cathodic shift in the voltammogram. This confirms the stability of the electrolytes in the studied potential range. The measured area of the micro electrode tips (from H-UPD) were 0.0022 and 0.0097 cm^2 for Ø = 500 and 250 μm electrodes, respectively. This translates to a roughness factor of 4.9 and 4.5, respectively.

3.2.2. Linear sweep voltammetry

Fig. 3B shows linear sweep voltammetry for Pt micro electrodes (Ø = 500 and 250 μm) in oxygen saturated and blanketed H_3PO_4 at 150 °C at 1 mV s^{-1}. It is clear that the current response is directly proportional to the electrode surface over the entire studied potential range. This is evident from the inset in Fig. 3B where the ORR current density (considering the measured UPD area) of both macro electrodes were almost identical. Fig. 3C shows linear sweep voltammetry for Pt micro electrodes (Ø = 250 μm) in oxygen saturated and blanketed H_3PO_4 and BPO_x at 150 °C at 1 mV s^{-1}. The obtained current densities in the early kinetic region to potentials down to 0.9 V (RHE) were very similar for H_3PO_4 and BPO_x, beyond which the performance of Pt in BPO_x was restricted by the oxygen mass transport, with a limiting current density of ca. 4 μA cm^{-2},; over an order of magnitude lower than that in H_3PO_4 (52 μA cm^{-2}). This is not a surprise since the BPO_x electrolyte is in the form of very thick slurry at the studied conditions which will result in very slow oxygen diffusion, in comparison to the liquid nature of H_3PO_4 under the same conditions. From Fig. 3C it is also evident that upon correcting for the oxygen transport limitation in BPO_x $[(j_L x j)/(j_L - j)]$, Pt showed identical performance in BPO_x and H_3PO_4 under the same conditions. The influence of oxygen mass transport will be discussed in more details in the next section.

Fig. 3D shows Tafel plots of steady state ORR on Pt in BPO_x and H_3PO_4 at 150 °C. As shown in the linear sweep voltammetry results, the ORR kinetic parameters in both electrolytes were very similar. The obtained Tafel slope was 90 ± 2 mV dec^{-1}, in very good agreement with the reported values for H_3PO_4 and highly doped PBI-H_3PO_4 systems at 150 °C [6,38,39]. To calculate the exchange current density, the Tafel slopes were extrapolated to the reversible cell voltage at 150 °C (gaseous water) of 1.158 V corrected for the oxygen solubility in H_3PO_4 of 1.07×10^{-4} mol L^{-1} [27] i.e. 1.106 V and in BPO_x of 1×10^{-3} mol L^{-1}(this work, sec 3.2.3) i.e. 1.127 V. The ORR exchange current density was therefore calculated to be 4×10^{-8} and 3×10^{-8} A cm$_{Pt}^{-2}$, respectively. The $j_{0\ Pt}$ in H_3PO_4 at 150 °C is in very good agreement with the reported values in the literature under comparable conditions 1.6×10^{-8} at 136 °C [40], 2.63×10^{-8} at 150 °C [27], 2.4×10^{-8} at 136 °C [41] and 6×10^{-8} A cm$_{Pt}^{-2}$ at 160 °C [39]. The similarity of ORR $j_{0\ Pt}$ for both H_3PO_4 and BPO_x combined with the slow gas diffusion through BPO_x and high ionic conductivities makes BPO_x an ideal membrane candidate for HT-PEMFC. It is therefore expected that membranes fabricated using BPO_x will outperform that of the typically used PBI-5 H_3PO_4 for HT-PEMFCs by offering a better ORR environment, since $j_{0\ Pt}$ in BPO_x is an order of magnitude higher that in PBI-5 H_3PO_4 at 150 °C. $j_{0\ Pt}$ values are reported to vary from 0.18 to 0.29 and

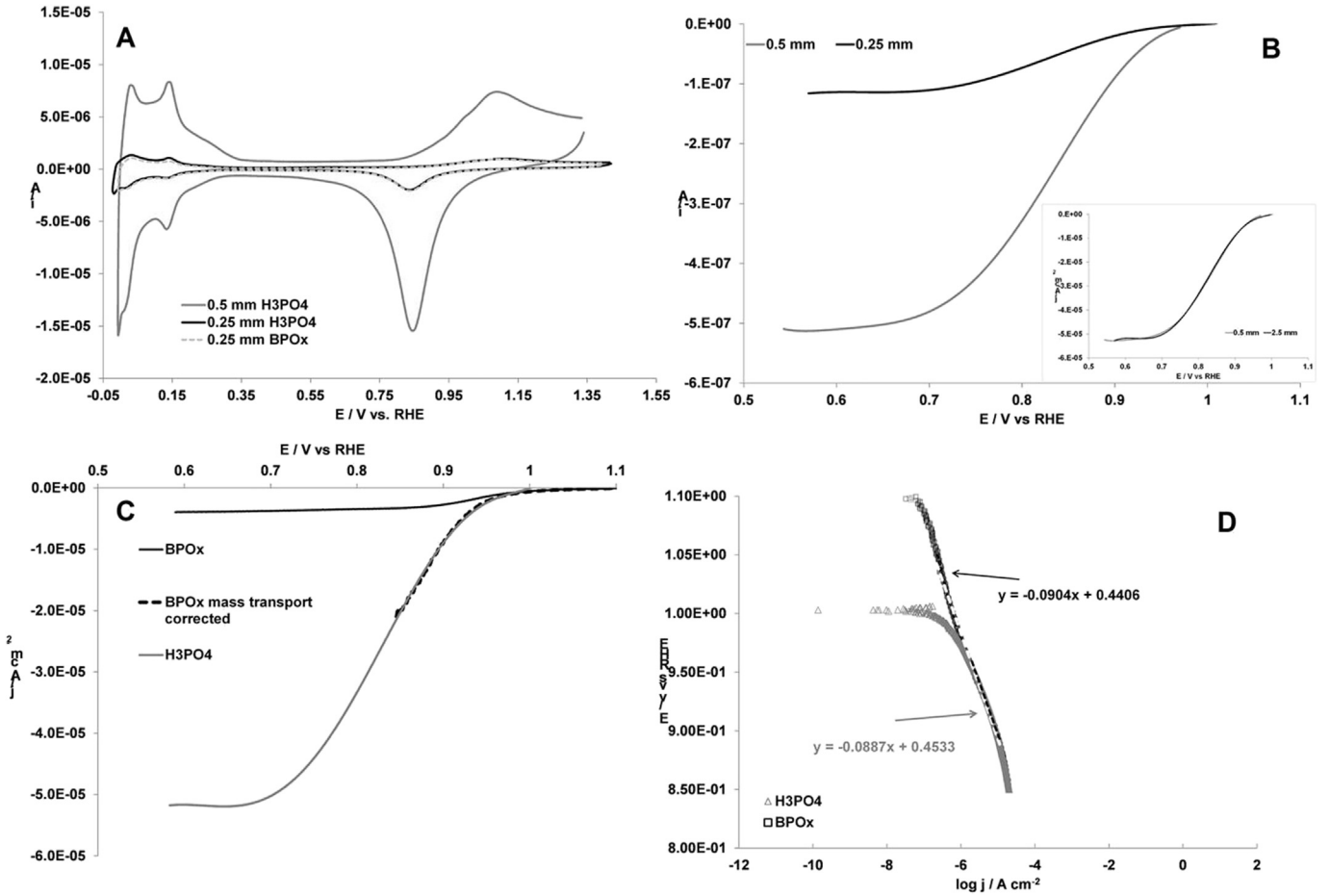

Fig. 3. (A) cyclic voltammogram of two Pt macro electrodes (Ø = 500 and 250 μm) in H_3PO_4 and BPO_x at 500 mV s^{-1}. (B) Linear sweep voltammetry for Pt micro electrodes (Ø = 500 and 250 μm) in oxygen saturated and blanketed H_3PO_4 at 150 °C at 1 mV s^{-1}, inset shows current density. (D) Linear sweep voltammetry for Pt micro electrodes (Ø = 250 μm) in oxygen saturated and blanketed H_3PO_4 and BPO_x at 150 °C at 1 mV s^{-1}. (E) Tafel plots of steady state ORR on Pt in BPO_x and H_3PO_4 at 150 °C.

2.4×10^{-8} A cm^{-2} with H_3PO_4 loadings of 4.5, 6 and 10 PRU, respectively, at 150 °C [38]. The $j_{0\ Pt}$ and transfer coefficient of ORR in PBI-H_3PO_4 systems depends on the H_3PO_4 content [42]. $j_{0\ Pt}$ increases with the increase H_3PO_4 content in PBI until it approaches that of pristine H_3PO_4 at high loadings (16 PRU).

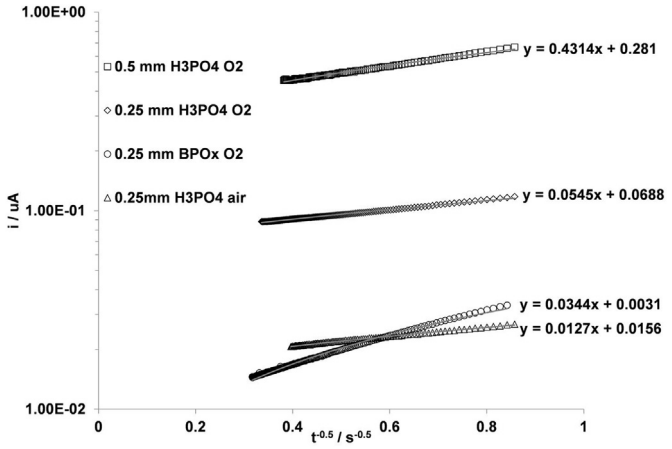

Fig. 4. I vs $t^{-0.5}$ plot for the mass transport limited ORR current transient after a potential step to 0.2 V (RHE) for 250 and 500 μm Ø electrodes from 1.5 to 10 s.

3.2.3. Chronoamperometry

The oxygen solubility and diffusion in H_3PO_4 and BPO_x were determined using chronoamperometry measurements. The limiting current under steady-state condition for micro electrode with radius r is given by Refs. [27,28]:

$$I_L = 4nFDcr \quad (6)$$

At short time periods the diffusion layer thickness is similar to (or smaller) the radius of the micro electrode and therefore diffusion is mainly planer at $\tau = 4Dt/r^2 < 3.2$, as time increases and the diffusion layer is sufficiently larger than the electrode's radius, the current at the electrode edge become significant (radial diffusion) and equation (2) becomes valid.

Fig. 4 shows a plot of I against $t^{-0.5}$ under mass transport controlled conditions with a fixed potential of 0.2 V (RHE) between 1.5 and 10 s. Values of D and C can be calculated using equation (2) from the slope and intercept of the fitted line. While equation (2) is not strictly accurate over the entire studied range under these experimental conditions ($\tau = 4Dt/r^2 < 3.2$, D_{O2} $H_3PO_4 = 3 \times 10^{-5}$ cm s^{-1} [27])), the obtained data is used as a guide in order to compare the results obtained here for C and D in H_3PO_4 with that reported in the literature for a similar micro electrode (Ø = 250 μm) study at 150 °C [27] in a similar time window.

The oxygen diffusion and solubility parameters are summarized in Table 1. The measured oxygen diffusion coefficient in H_3PO_4 at 150 °C using both electrodes (Ø = 250 & 500 μm) under oxygen and

Table 1
Oxygen diffusion coefficient and solubility at 150 °C in H_3PO_4 and BPO_x.

	DC Mole s^{-1} cm cm^{-2}	$D^{1/2}$ C	D cm^2 s^{-1}	C Mole cm^{-3}
Reported [27] H_3PO_4 O_2, 150 °C, 250 μm	3×10^{-12}	n/a	3.0×10^{-5}	1×10^{-7}
This work H_3PO_4 O_2, 150 °C, 500 μm	7.3×10^{-12}	1.2×10^{-9}	3.4×10^{-5}	2.1×10^{-7}
This work H_3PO_4 O_2, 150 °C, 250 μm	3.6×10^{-12}	6.3×10^{-10}	3.2×10^{-5}	1.1×10^{-7}
This work H_3PO_4 air, 150 °C, 250 μm	8.1×10^{-13}	1.5×10^{-10}	3.1×10^{-5}	2.6×10^{-8}
This work BPO_x O_2, 150 °C, 250 μm	1.6×10^{-13}	4×10^{-10}	1.6×10^{-7}	9.8×10^{-7}

air was ca. 3×10^{-5} cm s^{-1}; identical to that reported in the literature [27]. The oxygen solubility data varied between 1 and 2×10^{-7} mol cm^{-3} under oxygen also in very good agreement with the reported values in the literature [39–41,43].

From Table 1 it can be seen that the oxygen solubility in BPO_x is around an order of magnitude higher than that of H_3PO_4 (150 °C) i.e. 9.8×10^{-7} mol cm^{-3}. However, the oxygen diffusion coefficient in BPO_x is *ca.* two orders of magnitude lower than that in H_3PO_4 (150 °C), i.e. 1.6×10^{-7} cm s^{-1}.

As discussed earlier this is expected due to the high viscosity of BPO_x and is in agreement with the observed ratio of the limiting current (D.C) in both systems (an order of magnitude).

It can be seen from Fig. 4 that the intercept of the $I - t^{-0.5}$ line of 250 and 500 μm Ø electrodes (i.e. I_L for ORR in H_3PO_4) has a ratio of 4, this is in agreement with the data shown in Fig. 3B where the ratio of the limiting currents is also 4 for the same electrodes and the limiting current density of both electrodes are identical (Fig. 3B inset). This suggests that the limiting current is proportional to the electrode area and not the micro electrode radius as expected from equation (6). This means that oxygen diffusion under the studied conditions (diffusion coefficient, the studied time scale and micro electrode diameter) is mainly planer rather than radial diffusion. The diffusion layer thickness can be estimated, assuming planer diffusion, from the limiting current density j_L of *ca.* 5×10^{-5} A cm^{-2} (Fig. 3B inset & [27]) using [44]:

$$\frac{J_L}{nF} = \frac{-Dc}{\delta} \tag{7}$$

where δ is the diffusion layer thickness. δ is 230 μm considering values of $D_{O2\text{-}H3PO4} = 3 \times 10^{-5}$ cm s^{-1} and $C = 1 \times 10^{-7}$ mol cm^{-3} [27]. This value is in the range of the studied micro electrodes' radius, which confirms that radial diffusion is therefore negligible and is dominated by planer diffusion.

3.3. Fuel cell performance

Fig. 5 shows polarisation curves of the PEMFC utilising PBI-5.6H_3PO_4 (40 μm, 40 and 50%Pt/C) and BPO_x (110 μm, 30%Pt/C) using air (atm) at 150 °C at 0%RH. It is evident that BPO_x based MEA (30%Pt/C) outperformed that of PBI-5.6H_3PO_4 at low and medium current densities despite being ca. 3 times thicker. The low gas permeability through BPO_x (oxygen 1.6×10^{-13} mol cm cm^{-2} s^{-1}, Table 1) along with thicker membrane resulted in a significantly higher open circuit potential (ca. 100 mV) in comparison to PBI-5.6H_3PO_4. Oxygen (and hydrogen) permeability through PBI-5.6H_3PO_4 are between one to two orders of magnitude higher than that through BPO_x. For example: at 180 °C values are reported to be 900×10^{-13} and 3800×10^{-13} mol cm cm^{-2} s^{-1} for O_2 and H_2, respectively [45] and 21.8×10^{-13} mol cm cm^{-2} s^{-1} [38] for oxygen at 150 °C. The improvement is also visible in the kinetic region (ca. 69 mV), for example at 100 mA cm^{-2} the PBI based MEA voltage was 615 mV in comparison to 684 mV for BPO_x. The improvement is caused by lower fuel cross-over and higher ORR rate (j_0); over an order of magnitude in BPO_x in comparison to PBI-5.6H_3PO_4 as discussed in section 3.2.2. This is also visible in Fig. 6 inset, showing the IR-corrected polarisation curves (under O_2) plotted in logarithmic scale. The apparent Tafel slope was in the range of 90–100 mV dec^{-1} in agreement with the measured data in half cell tests. The exchange current density (based on electrode geometric

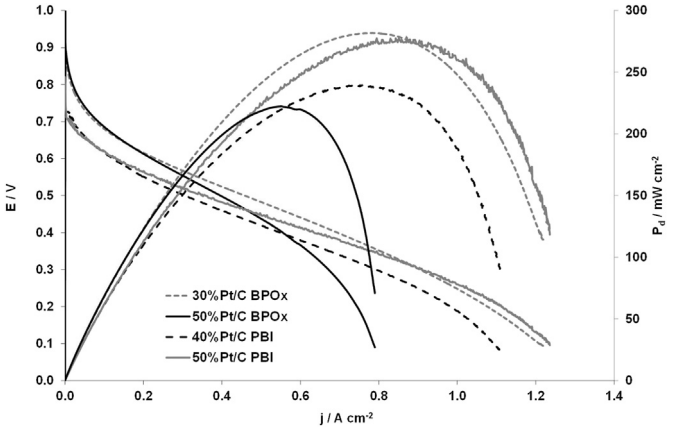

Fig. 5. Polarisation curves for MEAs utilizing 0.2 mg_{Pt} cm^2 anode 20%Pt/C and 0.4mg_{Pt} cm^2 cathodes (30, 40 or 50% Pt/C) using either membrane PBI-5.6pru 40 μm or BPO_x (250 μm 50%Pt/C and 110 μm 30%Pt/C) under 0%RH and Air (atm) at 150 °C.

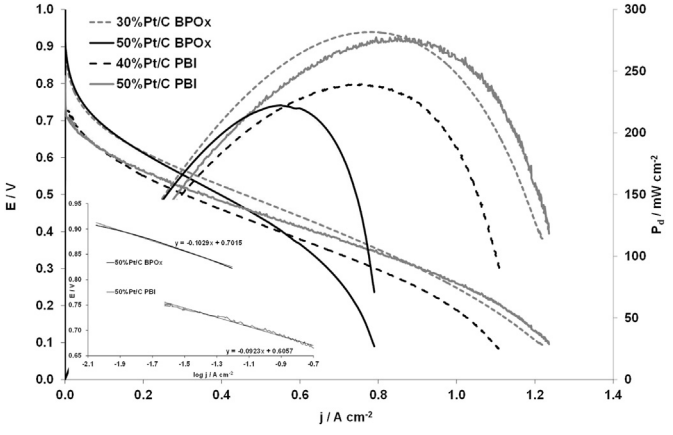

Fig. 6. Polarisation curves for MEAs utilizing 0.2 mg_{Pt} cm^2 anode 20%Pt/C and 0.4mg_{Pt} cm^2 cathodes (30, 40 or 50% Pt/C) using either membrane PBI-5.6pru 40 μm or BPO_x (250 μm 50%Pt/C and 110 μm 30%Pt/C) under 0%RH and O_2 (atm) at 150 °C. Inset: IR corrected Tafel slopes from polarisation curves using 50% Pt/C O_2 and 250 μm BPO_x.

area rather than Pt ESA) was calculated to be 130 and 4.4 × 10^{-6} A $cm^2_{geomtric}$ for BPO_x and PBI-5.6H_3PO_4, respectively. This translates in *ca*. 30 times faster ORR in BPO_x in comparison to PBI-5.6H_3PO_4.

For cathode loading of 0.6 mg_{Pt} cm^{-2} it was shown that the optimum cathode catalyst layer is achieved with 40%Pt/C and 50% Pt/C for PBI-5.6H_3PO_4 [19]. This will depend on the amount of the mobile electrolyte from the membrane to the electrodes and the electrolyte gas permeability. PBI with higher acid doping membranes typically requires 30%Pt/C [19], i.e. thicker catalyst layer. This is to enable better electrolyte distribution in the electrode and overall thinner average electrolyte film covering the catalyst particles enabling better gas transport to the catalyst. This is more critical in the case of BPO_x based electrolyte (in comparison to H_3PO_4) due to its low permeability to gases, while BPO_x is ideal for membrane materials, it might cause mass transport limitation when applied in the electrodes. The lower permeability of BPO_x is reflected in the lower limiting current (under air), *ca*. 0.8 A cm^{-2} in comparison to 1.3 A cm^{-2} in the case of PBI-5.6H_3PO_4 (when using 50%Pt/C). Upon increasing the catalyst layer thickness by utilising 30%Pt/C for BPO_x the mass transport in the electrode improved and a limiting current similar to that of PBI-5.6H_3PO_4 was achieved. The slope of the polarisation curves is affected by both mass transport rate and membrane conductivity. This is visible when comparing data from MEAs using 30 and 50% Pt/C on the cathode with BPO_4. It is therefore more accurate to measure the membrane resistance using impedance measurements. The membrane resistivity was 62 mΩ cm^2 for PBI-5.6H_3PO_4 in comparison to 79 mΩ cm^2 for BPO_x. This means that BPO_x is around 2.2 times more ionically conducting than PBI-5.6H_3PO_4 (since BPO_x membrane is 2.75 thicker) which is in agreement with the ex-situ conductivity measurements. At typical fuel cell operating potential of 0.6 V using BPO_x based MEA, an increased current density of 231 mA cm^{-2} (75% increase) in comparison to 132 mA cm^{-2} for PBI-5.6H_3PO_4 when using air (atm) was obtained.

The increase in current density at 0.6 V under oxygen (atm) is similarly significant from 425 to 706 mA cm^{-2}, a 66% increase when using BPO_x (Fig. 6). At 100 mA cm^{-2} the cell potential increased by 90 mV from 698 to 788 mV when using BPO_x instead of PBI-5.6H_3PO_4. Moreover, the peak power density reached a high value of 675 mW cm^{-2} under O_2 (atm) and ca.500 mW cm^{-2} under air (1 bar gauge) as shown in Fig. 7.

The OCP under air 1 bar (gauge) was ca. 1.0 V and the current density at 0.6 V (Fig. 7), shows an increase from 300 to 423 mA cm^{-2} when using BPO_x.

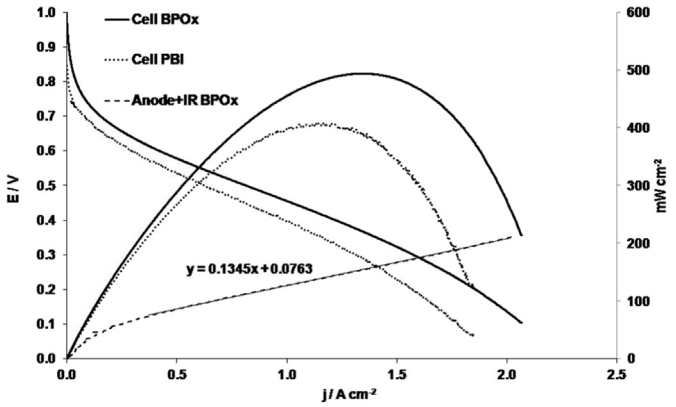

Fig. 7. Cell polarisation curves for MEAs utilizing 0.2 mg_{Pt} cm^2 anode 20%Pt/C and 0.4mg_{Pt} cm^2 cathodes 50% Pt/C with membrane PBI-5.6pru 40 μm and 30% Pt/C with BPO_x (110 μm) under 0%RH and air 1 bar (gauge) at 150 °C. Anode polarisation including membrane BPO_x IR (vs RHE) is also included.

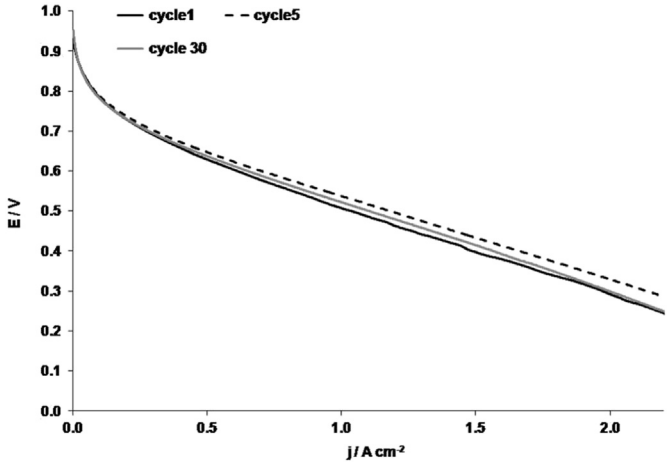

Fig. 8. Stability of BPO_x MEA after 30 cycles at 2 mV s^{-1} from OCP to 0 V (forward and backwards sweeps) at 150 °C under O_2 (atm) cycling using 50%Pt/C cathode and BPO_x (250 μm).

Finally, the stability of the BPO_x MEA was examined by repetitive cycling at 2 mV s^{-1} from OCP to 0 V and backwards over 30 cycles over a period of ca. 8.5 h. The first, fifth and thirtieth scans are shown in Fig. 8. It can be seen that no significant degradation occurred over the testing period. At 0.5 A cm^{-2} the cell potential varied from 637 to 647 to 629 in cycles 1 to 5 to 30. The change was in the range of ±10 mV within the experimental error of voltage/current measurements.

Overall the study shows that BPO_x is an attractive candidate for HT-PEMFC, offering lower gas permeability, higher OCP, higher ionic conductivity and a better environment for ORR than the typically used PBI-5.6H_3PO_4.

It should be mentioned that despite phosphoric acid fuel cells (PAFCs) having track record of thousands of hours of operation, recent studies have revealed that leaching of liquid PA from PBI based fuel cells and their catalyst layer causes inhomogeneous PA distribution that results in deterioration of the fuel cell performance during long-term operation [46–48]. The proposed BPOx-H_3PO_4 system here is still based on PA and is likely to suffer from the same leaching issues.

4. Conclusions

BPO_4 with excess of PO_4 (BPO_x) was synthesised and characterized for medium temperature fuel cell use (120–180 °C). The ionic conductivity was *ca*. 3 times higher than that of the typically used PBI-5.6H_3PO_4. The exchange current density for ORR in BPO_x is similar to that in H_3PO_4 of 3 × 10^{-8} A cm^{-2}_{Pt} in O_2 saturated solution at 150 °C. The value is over an order of magnitude higher than that reported in PBI-5.6H_3PO_4. MEA testing confirmed faster ORR rate in BPO_x (by 30×) in comparison to PBI-5.6H_3PO_4. BPO_x exhibits lower oxygen permeability; over an order of magnitude lower than that of PBI-5.6H_3PO_4, making it a material of choice for HT-PEMFCs membrane with recorded OCP ca. 1 V. However, the low oxygen permeability results in restricted oxygen transport to the cathode and thus to a lower limiting current of only 0.8 A cm^{-2} when using air (atm) with 50%Pt/C in comparison to > 1.2 A cm^{-2} when using PBI-5.6H_3PO_4. This limitation was mitigated by using a thicker cathode layer of 30%Pt/C ensuring better electrolyte distribution in the cathode catalyst layer and thinner average electrolyte film covering the catalyst particles. This resulted in a similar limiting current to PBI-5.6H_3PO_4 and a 75% increase in current density at 0.6 V, from 132 mA cm^{-2} in the case of PBI-5.6H_3PO_4 to

231 mA cm^{-2} in the case of BPO_x under air (atm).

Acknowledgements

The authors acknowledge the support of the EPSRC for funding under grant number EP/G030995. Solid-state NMR spectra were obtained at the EPSRC UK National Solid-state NMR Service at Durham.

References

[1] M. Mamlouk, K. Scott, Electrochimica Acta 56 (2011) 5493–5512.
[2] Q.F. Li, J.O. Jensen, R.F. Savinell, N.J. Bjerrum, Prog. Polym. Sci. 34 (2009) 449–477.
[3] J. Lobato, P. Canizares, M.A. Rodrigo, J.J. Linares, J.A. Aguilar, J. Membr. Sci. 306 (2007) 47–55.
[4] M. Mamlouk, K. Scott, J. Fuel Cell Sci. Technol. 8 (2011).
[5] S. Authayanun, M. Mamlouk, A. Arpornwichanop, Int. J. Hydrogen Energy 37 (2012) 6808–6817.
[6] M. Mamlouk, K. Scott, Proc. Institution Mech. Eng. Part A: J. Power Energy 225 (2011) 161–174.
[7] X. Wu, K. Scott, Fuel Cells 12 (2012) 583–588.
[8] M. Mamlouk, P. Ocon, K. Scott, J. Power Sources 245 (2014) 915–926.
[9] M. Mamlouk, K. Scott, Int. J. Hydrogen Energy 35 (2010) 784–793.
[10] M. Mamlouk, K. Scott, J. Power Sources 196 (2011) 1084–1089.
[11] S. Sanghi, M. Tuominen, E.B. Coughlin, Solid State Ionics 181 (2010) 1183–1188.
[12] S.J. Huang, H.K. Lee, W.H. Kang, Bull. Korean Chem. Soc. 26 (2005) 241–247.
[13] NASA Technical Brief, 69-10451, 1969.
[14] C.M. Ó'Laoire, in, Northeastern University, PhD thesis, Boston, 2010.
[15] K.C. Neyerlin, A. Singh, D. Chu, J. Power Sources 176 (2008) 112–117.
[16] Z.G. Qi, S. Buelte, J. Power Sources 161 (2006) 1126–1132.
[17] Q.F. Li, R. He, J.O. Jensen, N.J. Bjerrum, Fuel Cells 4 (2004) 147.
[18] K. Scott, M. Mamlouk, Battery Bimon. 36 (2006) 11.
[19] M. Mamlouk, K. Scott, Int. J. Energy Res. (2010), http://dx.doi.org/10.1002/er.1708.
[20] G. Alberti, M. Casciola, L. Massinelli, B. Bauer, J. Membr. Sci. 185 (2001) 73–81.
[21] P. Kmecl, P. Bukovec, Acta Chim. Slov. 46 (1999) 161–171.
[22] A. Baykal, M. Kizilyalli, M. Toprak, R. Kniep, Turkish J. Chem. 25 (2001) 425–432.
[23] S.D. Mikhailenko, J. Zaidi, S. Kaliaguine, J. Chem. Soc. Faraday Trans. 94 (1998) 1613–1618.
[24] S.D. Mikhailenko, S.M.J. Zaidi, E. Ghali, S. Kaliaguine, J. New Mater. Electrochem. Syst. 2 (1999) 161–169.
[25] E. Cho, J.S. Park, S.H. Park, Y.W. Choi, T.H. Yang, Y.G. Yoon, C.S. Kim, W.Y. Lee, S.B. Park, J. Membr. Sci. 318 (2008) 355–362.
[26] S.M.J. Zaidi, Electrochimica Acta 50 (2005) 4771–4777.
[27] B.R. Scharifker, P. Zelenay, J.O.M. Bockris, J. Electrochem. Soc. 134 (1987) 2714–2725.
[28] J.E. Baur, R.M. Wightman, J. Electroanal. Chem. Interfacial Electrochem. 305 (1991) 73–81.
[29] M. Mamlouk, K. Scott, J. Power Sources 196 (2010) 1084–1089.
[30] D. Peak, G.W. Luther Iii, D.L. Sparks, Geochimica Cosmochimica Acta 67 (2003) 2551–2560.
[31] R.d. Kniep, H. Engelhardt, C. Hauf, Chem. Mater. 10 (1998) 2930–2934.
[32] V.C. Farmer, The Infrared Spectra of Minerals, Mineralogical Society, 1974.
[33] W.W. Rudolph, Dalton Trans. 39 (2010) 9642–9653.
[34] E.A. Robinson, Can. J. Chem. 41 (1963) 173–179.
[35] K. Scott, S. Pilditch, M. Mamlouk, J. Appl. Electrochem. 37 (2007) 1245–1259.
[36] D.I. MacDonald, J.R. Boyack, J. Chem. Eng. Data 14 (1969) 380.
[37] Y.L. Ma, in, Case Western Reserve University, Cleveland, 2004.
[38] Z.Y. Liu, J.S. Wainright, M.H. Litt, R.F. Savinell, Electrochimica Acta 51 (2006) 3914–3923.
[39] H.R. Kunz, G.A. Gruver, J. Electrochem. Soc. 122 (1975) 1279–1287.
[40] A.J. Appleby, J. Electrochem. Soc. 117 (1970) 328–335.
[41] A.J. Appleby, J. Electroanal. Chem. Interfacial Electrochem. 24 (1970) 97.
[42] K. Scott, M. Mamlouk, Proc. IMechE Part A: J. Power Energy 225 (2011), http://dx.doi.org/10.1002/er.1708.
[43] J. McBreen, W.E. O'Grady, R. Richter, J. Electrochem. Soc. 131 (1984) 1215–1216.
[44] M. Mamlouk, K. Scott, J. Fuel Cell Sci. Technol. 8 (2011) article# 061003.
[45] R.H. He, Q.F. Li, A. Bach, J.O. Jensen, N.J. Bjerrum, J. Membr. Sci. 277 (2006) 38–45.
[46] G. Liu, H.M. Zhang, J.W. Hu, Y.F. Zhai, D.Y. Xu, Z.G. Shao, J. Power Sources 162 (2006) 547–552.
[47] M. Mamlouk, K. Scott, N. Hidayati, J. Fuel Cell Sci. Technol. 8 (2011) 1–8.
[48] Y. Oono, A. Sounai, M. Hori, J. Power Sources 189 (2009) 943–949.